



Deposited via The University of Leeds.

White Rose Research Online URL for this paper:

<https://eprints.whiterose.ac.uk/id/eprint/146355/>

Version: Accepted Version

Article:

Sadeghi, Z, Valadan Zoej, MJ, Hooper, A et al. (2018) A New Polarimetric Persistent Scatterer Interferometry Method Using Temporal Coherence Optimization. IEEE Transactions on Geoscience and Remote Sensing, 56 (11). pp. 6547-6555. ISSN: 0196-2892

<https://doi.org/10.1109/TGRS.2018.2840423>

© 2018 IEEE. This is an author produced version of a paper published in IEEE Transactions on Geoscience and Remote Sensing. Personal use of this material is permitted. Permission from IEEE must be obtained for all other uses, in any current or future media, including reprinting/republishing this material for advertising or promotional purposes, creating new collective works, for resale or redistribution to servers or lists, or reuse of any copyrighted component of this work in other works. Uploaded in accordance with the publisher's self-archiving policy.

Reuse

See Attached

Takedown

If you consider content in White Rose Research Online to be in breach of UK law, please notify us by emailing eprints@whiterose.ac.uk including the URL of the record and the reason for the withdrawal request.

A New Polarimetric Persistent Scatterer Interferometry Method using Temporal Coherence Optimization

Zahra Sadeghi¹, Mohammad Javad Valadan Zoej¹, Andrew Hooper², *Senior Member, IEEE*, Juan M. Lopez Sanchez³, *Senior Member, IEEE*

⁽¹⁾ Faculty of Geomatics and Geodesy, K.N.Toosi University of Technology, Tehran, Iran.

⁽²⁾ COMET, School of Earth and Environment, University of Leeds, Leeds, UK.

⁽³⁾ Department of Physics, System Engineering and Signal Theory, University of Alicante, Alicante, Spain.

Corresponding author: Zahra Sadeghi, a.zahra.sadeghi@gmail.com

Abstract- While polarimetric Persistent Scatterer InSAR (PSI) is an effective technique for increasing the number and quality of selected persistent scatterer (PS) pixels, existing methods are suboptimal; a polarimetric channel combination is selected for each pixel based either on amplitude, which works well only for high amplitude scatterers such as man-made structures, or on the assumption that pixels in a surrounding window all have the same scattering mechanism. In this study, we present a new polarimetric PSI method in which we use a phase-based criterion to select the optimal channel for each pixel, which can work well even in non-urban environments. This algorithm is based on polarimetric optimisation of temporal coherence, as defined in the Stanford Method for Persistent Scatterers (StaMPS), to identify scatterers with stable phase characteristics. We form all possible co-polar and cross-polar interferograms from the available polarimetric channels and find the optimum coefficients for each pixel using defined search spaces to optimise the temporal coherence. We apply our algorithm, PolStaMPS, to an area in the Tehran basin that is covered primarily by vegetation. Our results confirm that the algorithm substantially improves on StaMPS performance, increasing the number of PS

25 **pixels by 48%, 80% and 82% with respect to HH+VV, VV and HH channel, respectively,**
26 **and increasing the signal-to-noise ratio of selected pixels.**

27 **Keywords:** polarimetric Persistent Scatterer InSAR, StaMPS, temporal coherence.

28 1. INTRODUCTION

29 Persistent Scatterer InSAR (PSI) is a well-known technique to address decorrelation and
30 atmospheric noise in conventional interferometry. This method identifies only those scatterers
31 which display coherent scattering behaviour over time, known as persistent scatterers. A PSI
32 algorithm was outlined first by Ferretti *et al.* [1], [2] with further algorithms quickly following
33 [3], [4], [5] and [6]. In these algorithms, an initial set of PS pixels are identified by analysis of
34 their amplitude scintillations in a series of co-registered SLC images and then refined based on
35 the match of their phase with a pre-defined deformation model. Thus, in general, only bright
36 scatterers with a deformation behaviour close to the assumed model are identified as PS pixels,
37 and these algorithms work best where there are large numbers of man-made structures.
38 Moreover, small baseline SAR differential interferometry approaches were presented by [7]
39 and [8] based on appropriate combination of different interferograms produced by data pairs
40 with small orbital separation (baseline) in order to limit the spatial decorrelation. In these
41 methods, coherent pixels are selected through spatial coherence estimation.

42 An alternative PSI method, was put forward by [9] to identify large numbers of PS pixels in all
43 terrains, including non-urban areas that lack man-made structures. This approach uses the
44 spatial correlation of phase for identification of PS pixels. The parameter used to characterize
45 phase stability in this approach is similar to a measure of coherence in time [10] and we refer
46 to it as temporal coherence [9]. The ensemble phase coherence defined by [2], is not quite the
47 same as the temporal coherence we refer to, as it requires a predefined deformation model.

48 Before the launch of radar sensors operating with a polarimetric configuration, SAR
49 interferometry applications had been limited to a single polarimetric channel. Radar

50 polarimetry is a valuable technique for the extraction of geophysical parameters from SAR
51 images [11] and [12]. Varying approaches to achieve this are based either on the statistical
52 analysis of the polarimetric information [13] , [14] or on scattering models, which provide an
53 understanding of the physics of the scattering process [15] , [16] and [17]. Therefore the
54 introduction of polarimetric techniques in interferometric applications can improve
55 performance of SAR interferometry. A general formulation for coherent conventional
56 interferometry using polarimetry was introduced by Cloude and Papathanassiou [18]. This
57 method sets up a spatial coherence optimisation problem using different polarimetric channels
58 and then solves it to obtain the optimum linear combination of channels that leads to the best
59 phase estimates. The decorrelation terms are decreased with the spatial coherence optimisation,
60 and signal-to-noise ratio is therefore increased [19]. Another spatial coherence optimisation
61 method was proposed by Colin *et al.*, [20]. This approach optimises the coherence using the
62 same complex unitary vector for both antennae. This coherence is called single-mechanism
63 coherence. Given a multi-baseline data set in this method, coherence can be optimised
64 independently for every baseline. This can lead to identification of different dominant
65 scattering centres depending on the chosen baseline. A more robust polarimetric optimisation
66 approach to find the most coherent and dominant scatterer is a simultaneous optimisation of
67 multi-baseline coherence, a technique first outlined by Neumann *et al.*, [19]. This approach
68 generally leads to lower coherence magnitudes, but the corresponding linear combination of
69 channels and their interferometric phases are estimated on the basis of all the available data
70 and thus more accurately.

71 As density and quality of PS pixels are important factors in PSI algorithms, the concept of
72 polarimetric optimisation in the PSI algorithms was proposed in [21] and [22] with zero-
73 baseline ground based SAR (GB-SAR) data, to improve the number of reliable pixel
74 candidates. In [21], the simplest coherence optimisation approach is performed based on

75 selection of the polarimetric channel with the highest average coherence value. A polarimetric
76 PSI approach, known as ESPO (Exhaustive Search Polarimetric Optimisation), using
77 spaceborne data set was presented first by Navarro-Sanchez *et al.*, [23]. This method finds the
78 optimal weights for each available polarimetric channel to obtain an optimum combination of
79 those channels that maximises the PS selection criterion. A study of the different polarimetric
80 optimisation techniques using both zero-baseline and multi-baseline data was carried out by
81 Iglesias *et al.*, [24]. The main goal was the exploitation of the available polarimetric
82 optimisation methods, in the framework of differential interferometry, to improve the density
83 and quality of PS pixels. Moreover, Sadeghi *et al.*, compared the efficiency of different multi-
84 baseline polarimetric optimisation techniques in terms of increasing the number of PS pixels
85 and the signal-to-noise ratio, and also presented an enhanced multi-baseline coherence
86 optimisation method [25]. It should be noted that the use of polarimetric SAR data entails two
87 main drawbacks when compared to conventional single-polarimetric data: an increase in the
88 amount of data to be processed (proportional to the number of polarimetric channels) and a
89 reduction in the size of the images in the swath direction (hence the spatial coverage) due to
90 the doubled pulse repetition frequency required to acquire fully polarimetric data.

91 Polarimetric PSI implementations, up to now, either optimise amplitude-based criteria for
92 identification of PS pixels [23] , [24] , [26] and [27], or select the polarimetric channel
93 combination that maximises the ensemble coherence of surrounding pixels [26] , [25] and [24].
94 The former approach can be quite successful for bright scatterers, such as buildings, but less
95 for natural PS. A limitation of the latter approach is the common failure of the assumption that
96 PS pixels are surrounded by scatterers with the same scattering properties, which leads to non-
97 optimal weights for the polarimetric channels, and to a loss of spatial resolution. In this paper,
98 we present a new method, PolStaMPS (Polarimetric StaMPS), which uses polarimetric
99 optimisation of temporal coherence to increase the number of selected PS pixels in all terrains,

100 with or without buildings. We implement the temporal coherence optimisation after computing
101 different interferogram channels for each master and slave image. The temporal coherence
102 optimisation method was inspired by ESPO, as it finds the weights for each interferogram
103 channels over search spaces. PolStaMPS codes will be included in the next release of
104 StaMPS/MTI, with full instructions added to the manual.

105 This paper is organised as follows. Section 2 contains the basic principles of polarimetric
106 interferometry and a brief review of ESPO, which is a polarimetric persistent scatterer
107 interferometry method. The concept of temporal coherence in StaMPS is introduced in Section
108 3, followed by our new algorithm for optimisation of the temporal coherence, PolStaMPS, in
109 Section 4. Section 5 describes the test site and the available dual polarimetric data set to
110 evaluate the new algorithm. In Section 6, experimental results of PolStaMPS are shown and
111 discussed. Finally, the main conclusions are summarized in Section 7.

112 **2. POLARIMETRIC INTERFEROMETRY**

113 Since there is a vector value for each pixel instead of a scalar one, polarimetric interferometry
114 can be referred to as vector interferometry [18]. The general formulation is defined in Section
115 2.1. One of the most effective polarimetric PSI algorithms up to now, ESPO, was presented in
116 [26]. This technique was formulated for two different criteria of PS selection to increase the
117 number of PS pixels, which are amplitude dispersion index and average spatial coherence. A
118 brief overview of this method is presented in Section 2.2.

119 **2.1 GENERAL FORMULATION**

120 A general formulation for polarimetric SAR interferometry, presented in full by Cloude and
121 Papathanassiou [18], is reviewed in this section. Fully polarimetric radar systems measure a
122 2×2 complex scattering matrix $[S]$ for each pixel in an image [28]. Through vectorization of
123 the scattering matrix, a coherent scattering vector \underline{k} can be extracted to generalise

124 interferometric phase and spatial coherence. Using Pauli basis matrices, the scattering vector
 125 for each pixel can be found as [18]

$$126 \quad \underline{k} = \frac{1}{\sqrt{2}} [S^{HH+VV}, S^{HH-VV}, 2S^{HV}]^T, \quad (1)$$

127 where T indicates the matrix transposition operation, and S^{ij} ($i, j = H$ or V) is the complex
 128 scattering coefficient for j transmitted and i received polarization in the HV polarisation basis.

129 In the case of dual-polarisation interferometry, considering there is no data from the cross-polar
 130 channel, as provided by TerraSAR-X, the scattering vector changes to

$$132 \quad \underline{k} = \frac{1}{\sqrt{2}} [S^{HH+VV}, S^{HH-VV}]^T. \quad (2)$$

133 Using the outer product formed from the scattering vectors \underline{k}_m and \underline{k}_s for master and slave
 134 images, a 4×4 matrix can be defined,

$$136 \quad \mathbf{T}_4 = \begin{bmatrix} \mathbf{T}_{mm} & \Omega_{ms} \\ \Omega_{ms}^H & \mathbf{T}_{ss} \end{bmatrix}, \quad (3)$$

137 where H stands for conjugate transpose, and \mathbf{T}_{mm} , \mathbf{T}_{ss} and Ω_{ms} are 2×2 complex matrices
 138 given by

$$139 \quad \mathbf{T}_{mm} = \langle \underline{k}_m \underline{k}_m^H \rangle$$

$$140 \quad \mathbf{T}_{ss} = \langle \underline{k}_s \underline{k}_s^H \rangle$$

$$141 \quad \Omega_{ms} = \langle \underline{k}_m \underline{k}_s^H \rangle. \quad (4)$$

142 In order to extend standard SAR interferometry, which uses a scalar formulation, into a vector
 143 formulation, two normalised complex vectors $\underline{\omega}_m$ and $\underline{\omega}_s$ for master and slave images, are
 144 introduced. These vectors can be called projection vectors and interpreted as linear combination
 145 of channels. The scalar complex value for each pixel can be defined as $\mu = \underline{\omega}^H \underline{k}$, which is a
 146 linear combination of the elements of \underline{k} . The vector interferogram is obtained as

147
$$\mu_m \mu_s^* = (\underline{\omega}_m^H \underline{k}_m) (\underline{\omega}_s^H \underline{k}_s)^H = \underline{\omega}_m^H \Omega_{ms} \underline{\omega}_s,$$

148 (5)

149 where * is the conjugate operation. The interferometric phase can be extracted using

150
$$\varphi_{int} = \arg(\underline{\omega}_m^H \Omega_{ms} \underline{\omega}_s). \quad (6)$$

151 Optimum values of the projection vectors can be found through polarimetric optimisation of
 152 spatial coherence. The generalised vector expression for the spatial coherence ρ is given by

153
$$\rho = \frac{|E(\underline{\omega}_m^H \Omega_{ms} \underline{\omega}_s)|}{\sqrt{E(\underline{\omega}_m^H \mathbf{T}_{mm} \underline{\omega}_m) E(\underline{\omega}_s^H \mathbf{T}_{ss} \underline{\omega}_s)}},$$

154 (7)

155 where $E(\dots)$ indicates the expectation operator. In order to estimate the spatial coherence, a
 156 window is required and it is assumed that the surrounding pixels in the window have similar
 157 scattering properties. Therefore, in addition to the loss of the spatial details, the optimisation
 158 process will not work properly in the common case where this is not true.

159 The $\underline{\omega}$ vector can be constrained to be the same all along the whole stack of images. This is
 160 referred to as Equal Scattering Mechanisms (ESM), which selects the most stable scattering
 161 mechanism over time for each pixel of an image set covering a case study [26]. Moreover, in
 162 the case of multi-baseline spatial coherence optimisation, the averaged spatial coherence, $\bar{\rho}$, is
 163 optimised according to (8).

164
$$|\bar{\rho}| = \frac{1}{K} \sum_{k=1}^K |\rho_k|,$$

165 (8)

166 where K is the number of interferometric pairs.

167 2.2 ESPO

168 Polarimetric PSI was first introduced by Navarro-Sanchez *et al.* in [23] through ESPO, which
 169 is a multi-baseline ESM optimisation method. This optimisation approach consists of searching
 170 for the unitary vector $\underline{\omega}$ that maximises the PS selection criteria, which can be either average

171 spatial coherence or amplitude dispersion index. The optimum interferogram can be found with
 172 a parametrisation of $\omega(\alpha, \psi)$, in the case of dual-polarimetry, as

$$173 \quad \underline{\omega} = [\cos \alpha, \sin \alpha e^{j\psi}]^T, \begin{cases} 0 \leq \alpha \leq \pi/2 \\ -\pi \leq \psi < \pi \end{cases}$$

174
175 (9)

176 This parametrisation of the projection vector assumes that it is unitary, $|\underline{\omega}| = 1$, and rotated
 177 such that the phase of the first element is zero. Through an exhaustive search, optimum values
 178 are found for α and ψ for each pixel. The α parameter we define here should not be confused
 179 with the α angle widely used in polarimetry after its definition in [17].

180 After optimisation of the quality criteria, PS pixels are selected based on a threshold average
 181 spatial coherence in multi-looked data, or a threshold amplitude dispersion index in single-
 182 looked data. More recently, the amplitude dispersion index was optimised through ESPO to
 183 improve the PS analysis in [27]. Moreover, an alternative way to optimise the coherence was
 184 proposed to decrease the computation time [29].

185 3. TEMPORAL COHERENCE IN StaMPS

186 StaMPS is a PSI technique designed to work in non-urban environments, with deformation that
 187 may be highly non-linear in time. The PS identification step in this method is based primarily
 188 on phase characteristics and can identify low-amplitude pixels more effectively than traditional
 189 amplitude-based algorithms [9].

190 The main criterion of PS identification, temporal coherence, is estimated using phase analysis.

191 After forming interferograms and removing most of topographic phase, the residual phase of
 192 the x th pixel in the k th interferogram, $\varphi_{int,x,k}$, contains a contribution from several sources as

$$193 \quad \varphi_{int,x,k} = \varphi_{def,x,k} + \varphi_{\alpha,x,k} + \varphi_{orb,x,k} + \varphi_{\epsilon,x,k} + \varphi_{n,x,k},$$

194 (10)

195 where $\varphi_{def,x,k}$ is the phase change due to deformation in the satellite line-of-sight (LOS)
 196 direction, $\varphi_{\alpha,x,k}$ is the phase due to difference in atmospheric delay between passes, $\varphi_{orb,x,k}$ is

197 the phase due to orbit inaccuracies, $\varphi_{\varepsilon,x,k}$ is the residual topographic phase due to error in the
 198 DEM, and $\varphi_{n,x,k}$ is the decorrelation noise term.

199 Quantification of the noise term is used to identify which scatterers are persistent [30].

200 Assuming spatial correlation of most of phase contributions over a specified distance, the
 201 spatial average of residual phase, $\bar{\varphi}_{int,x,k}$, is estimated using a spatial filtering as

$$202 \quad \bar{\varphi}_{int,x,k} = \bar{\varphi}_{def,x,k} + \bar{\varphi}_{\alpha,x,k} + \bar{\varphi}_{orb,x,k} + \bar{\varphi}_{\varepsilon,x,k}, \quad (11)$$

203 where the bar denotes the spatially filtered phase, and $\bar{\varphi}_{\varepsilon,x,k}$ is the spatially filtered sum of
 204 $\varphi_{\varepsilon,x,k}$ and $\varphi_{n,x,k}$. Subtracting the spatially correlated phase, equation (11), from residual phase,
 205 equation (10), yields

$$207 \quad \varphi_{int,x,k} - \bar{\varphi}_{int,x,k} = \varphi_{\varepsilon,x,k} + \varphi_{n,x,k} - \bar{\varphi}'_{\varepsilon,x,k}, \quad (12)$$

208 where $\bar{\varphi}'_{\varepsilon,x,k} = \bar{\varphi}_{\varepsilon,x,k} - (\varphi_{def,x,k} - \bar{\varphi}_{def,x,k}) - (\varphi_{\alpha,x,k} - \bar{\varphi}_{\alpha,x,k}) - (\varphi_{orb,x,k} - \bar{\varphi}_{orb,x,k})$,

209 and is assumed to be insignificant. The residual topography phase is proportional to the
 210 perpendicular component of the baseline, $B_{\perp,x,k}$, so $\varphi_{\varepsilon,x,k} = B_{\perp,x,k} G_{\varepsilon,x}$ where $G_{\varepsilon,x}$ is a
 211 proportionality constant that can be estimated. Temporal coherence, which is a measure of
 212 phase noise level and indicator of whether the pixel is a PS [30] and [31], is defined as follows

$$214 \quad \gamma_x = \frac{1}{K} \left| \sum_{k=1}^K \exp\{\sqrt{-1} (\varphi_{int,x,k} - \bar{\varphi}_{int,x,k} - \hat{\varphi}_{\varepsilon,x,k})\} \right|, \quad (13)$$

215 where K is the number of available interferograms and $\hat{\varphi}_{\varepsilon,x,k}$ is the estimate of residual
 216 topographic phase. For each PS candidate, $\bar{\varphi}_{int,x,k}$, $\hat{\varphi}_{\varepsilon,x,k}$ and relevant γ_x are estimated in an
 217 iterative process until temporal coherence convergence is achieved. Finally, PS pixels are
 218 selected based on the probability that their phase time series is not just noise, by comparing
 219 the joint probability density function (PDF) of coherence and amplitude dispersion index to
 220 that for simulated pixels with random phase.

222

223

4. TEMPORAL COHERENCE OPTIMISATION IN PolStaMPS

All polarimetric PSI algorithms to date have utilised spatial coherence or the amplitude dispersion index to optimise the weights for the different polarimetric channels. Amplitude-based polarimetric PSI is only useful for high amplitude PS. On the other hand, using spatial coherence to select PS pixels relies on surrounding pixels having the same mechanism, which is often not the case for PS pixels.

In our new algorithm we extend the approach of StaMPS, which uses temporal coherence to select PS with high-density in non-urban areas. The main goal of the algorithm is to find the weights for the polarimetric channels that optimise the temporal coherence for each pixel. In addition to optimising the phase-based criterion, implementing the optimisation process after forming interferograms and removing the topographic contribution is a difference of PolStaMPS compared to other polarimetric PSI algorithms.

The optimum interferogram phase, $\varphi_{opt-int,x,k}$, obtained from substituting equation (2) in equation (5) is

$$\begin{aligned}
 \varphi_{opt-int,x,k} &= \arg(\underline{\omega}_m^H \Omega_{ms} \underline{\omega}_s) \\
 &= \arg\left(\frac{1}{2} \begin{bmatrix} \omega_m^{i*} & \omega_m^{ii*} \end{bmatrix} \begin{bmatrix} S_m^{HH+VV} \cdot S_s^{HH+VV*} & S_m^{HH+VV} \cdot S_s^{HH-VV*} \\ S_m^{HH-VV} \cdot S_s^{HH+VV*} & S_m^{HH-VV} \cdot S_s^{HH-VV*} \end{bmatrix} \begin{bmatrix} \omega_s^i \\ \omega_s^{ii} \end{bmatrix}\right) \\
 &= \arg\left(f_1 \cdot \frac{1}{2} (S_m^{HH+VV} \cdot S_s^{HH+VV*}) + f_2 \cdot \frac{1}{2} (S_m^{HH+VV} \cdot S_s^{HH-VV*}) + f_3 \cdot \frac{1}{2} (S_m^{HH-VV} \cdot S_s^{HH+VV*}) \right. \\
 &\quad \left. + f_4 \cdot \frac{1}{2} (S_m^{HH-VV} \cdot S_s^{HH-VV*})\right) \\
 &= \arg(f_1 \cdot \Phi_{int-1,x,k} + f_2 \cdot \Phi_{int-2,x,k} + f_3 \cdot \Phi_{int-3,x,k} + f_4 \cdot \Phi_{int-4,x,k}), \tag{14}
 \end{aligned}$$

where $\Phi_{int-1,x,k} \dots \Phi_{int-4,x,k}$, elements of $[\Omega_{ms}]$, are 4 different types of interferogram, whose linear combination forms the optimum k th interferogram for the x th pixel. ω^i and ω^{ii} are the first and second element of $\underline{\omega}$. $f_1 \dots f_4$ are coefficients for the 4 types of interferogram as

$$\begin{aligned}
 f_1 &= \omega_m^{i*} \cdot \omega_s^i \\
 f_2 &= \omega_m^{ii*} \cdot \omega_s^i
 \end{aligned}$$

$$\begin{aligned}
251 \quad & f_3 = \omega_m^{i*} \cdot \omega_s^{ii} \\
252 \quad & f_4 = \omega_m^{ii*} \cdot \omega_s^{ii} \\
253 \quad & (15)
\end{aligned}$$

254 The polarimetric expression of temporal coherence is introduced in (16). Similar to
255 standard StaMPS, there is an iterative process to estimate $\bar{\varphi}_{opt-int,x,k}$, which is
256 substituted by the spatially correlated phase of $\Phi_{int-1,x,k}$ in the first iteration. In
257 every iteration, after applying a spatial filtering to calculate $\bar{\varphi}_{opt-int,x,k}$, the
258 optimum values for $f_1 \dots f_4$ and $\hat{\varphi}_{\varepsilon,x,k}$ are found in the defined search spaces to
259 optimise $\gamma_{pol,x}$ and then the final value of the $\hat{\varphi}_{\varepsilon,x,k}$ is estimated through the
260 obtained optimum phase. In the final iteration, polarimetric temporal coherence
261 converges, and the coefficients and the optimum interferograms, according to (14),
262 are obtained.

$$\begin{aligned}
263 \quad \gamma_{pol,x} &= \frac{1}{K} \left| \sum_{k=1}^K \exp\{\sqrt{-1}(\varphi_{opt-int,x,k} - \bar{\varphi}_{opt-int,x,k} - \hat{\varphi}_{\varepsilon,x,k})\} \right| \\
264 \quad & (16)
\end{aligned}$$

265 In order to optimise $\gamma_{pol,x}$, the coefficients are parametrised based on the definition of $\underline{\omega}$ in
266 ESPO as

$$\begin{aligned}
267 \quad & f_1 = \cos \alpha \cdot \cos \alpha = \cos^2 \alpha \\
268 \quad & f_2 = \sin \alpha e^{-j\psi} \cdot \cos \alpha = \sin \alpha \cdot \cos \alpha \cdot e^{-j\psi} \\
269 \quad & f_3 = \cos \alpha \cdot \sin \alpha e^{j\psi} = \cos \alpha \cdot \sin \alpha e^{j\psi} \\
270 \quad & f_4 = \sin \alpha e^{-j\psi} \cdot \sin \alpha e^{j\psi} = \sin^2 \alpha \\
271 \quad & (17)
\end{aligned}$$

272 Therefore, only a two-dimensional search space is defined by α and ψ in each iteration, and the
273 best values are extracted for each one. In order to define coefficients and then optimise the
274 temporal coherence, we specified a grid for the search space of α and ψ values, with 10 degrees
275 steps. Steps larger than 10 degrees would yield a shorter computing time, but due to the
276 relatively complex pattern of the temporal coherence function, may cause convergence on a
277 local maximum rather than the absolute one.

278

279 **5. CASE STUDY AND DATA SET**

280 Since the main priority of this research is increasing PS density in non-urban areas, we selected
281 Tehran basin, which contains areas primarily covered by vegetation, as a test case. The Tehran
282 basin suffers from a high-rate of land subsidence and is located in the north of Iran, between
283 the Alborz Mountains to the north and the Arad and Fashapouye mountains to the south. This
284 subsidence was first revealed by geodetic observations from precise levelling surveys carried
285 out across the area between 1995 and 2002 [32]. Due to poor coherence, conventional
286 interferometry has generally not been successful in measuring deformation. Therefore, a
287 number of enhanced algorithms based on PSI have been applied to this region [33], [34] and
288 [35]. We applied our new PolStaMPS method to a 2.6×1.2 km portion of the Tehran basin
289 containing pixels with the highest rate of deformation and covered mostly by agricultural fields
290 (Figure 1).

291

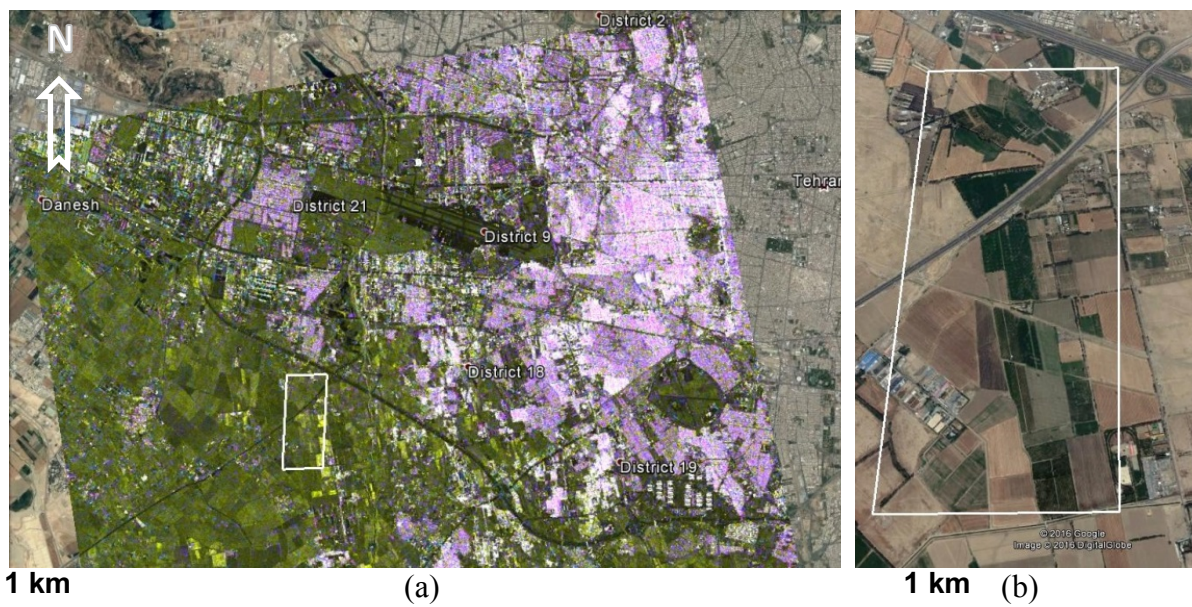


Fig. 1 (a) Spatial location of the case study (outlined polygon) over the composite RGB of master image (20131211), Channels: R=HH, G=VV, B: Absolute value of the difference between channels. (b) The case study (outlined rectangle) with detailed features.

292

293 In order to optimise the temporal coherence using polarimetric data, we tasked TerraSAR-X to
 294 acquire dual-polarisation (HH/VV) images. A set of 22 dual-polarisation Strip-map images
 295 from 21 July 2013 to 22 April 2014 were obtained. Azimuth and slant-range resolution are 6.6
 296 and 1.17 m, respectively, whereas pixel dimensions are 2.4 and 0.91 m, respectively. Fig. 2
 297 illustrates the spatial and temporal baselines of all slave images with respect to the master one.

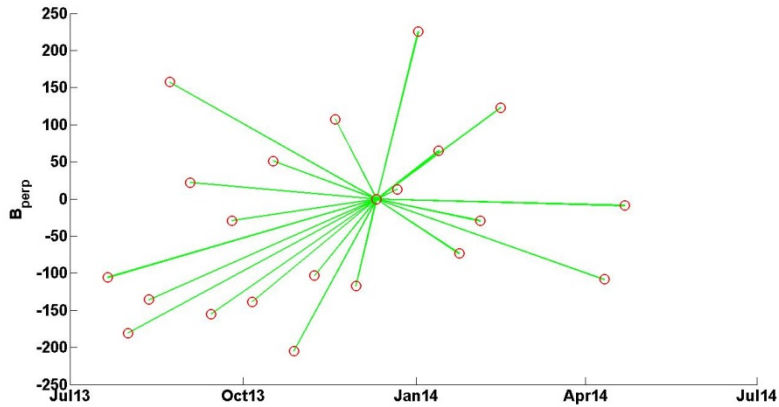


Fig. 2. Spatial baselines vs. temporal baselines of slave images with respect to the master (20131211).

298

299

6. PolStaMPS RESULTS AND DISCUSSION

300 In addition to the linear channels (HH and VV), we also ran StaMPS on the HH+VV channel,
 301 which forms the initial co-polar interferogram in PolStaMPS, $\Phi_{int-1,x,k}$, as its phase values
 302 are expected to be more stable over surface scattering areas, e.g. rural ones, than the linear
 303 channels.

304 Figure 3 displays the polarimetric temporal coherence values as a function of (α, ψ) for four
 305 representative pixels with different values of optimum temporal coherence. The shape of the
 306 temporal coherence function is smooth enough to allow numerical methods to approximate the
 307 maximum value. For this reason, a point close to the absolute maximum of the temporal
 308 coherence is first found using a grid search, and then a gradient-based method is used to find
 309 the maximum, hence reducing the computational cost.

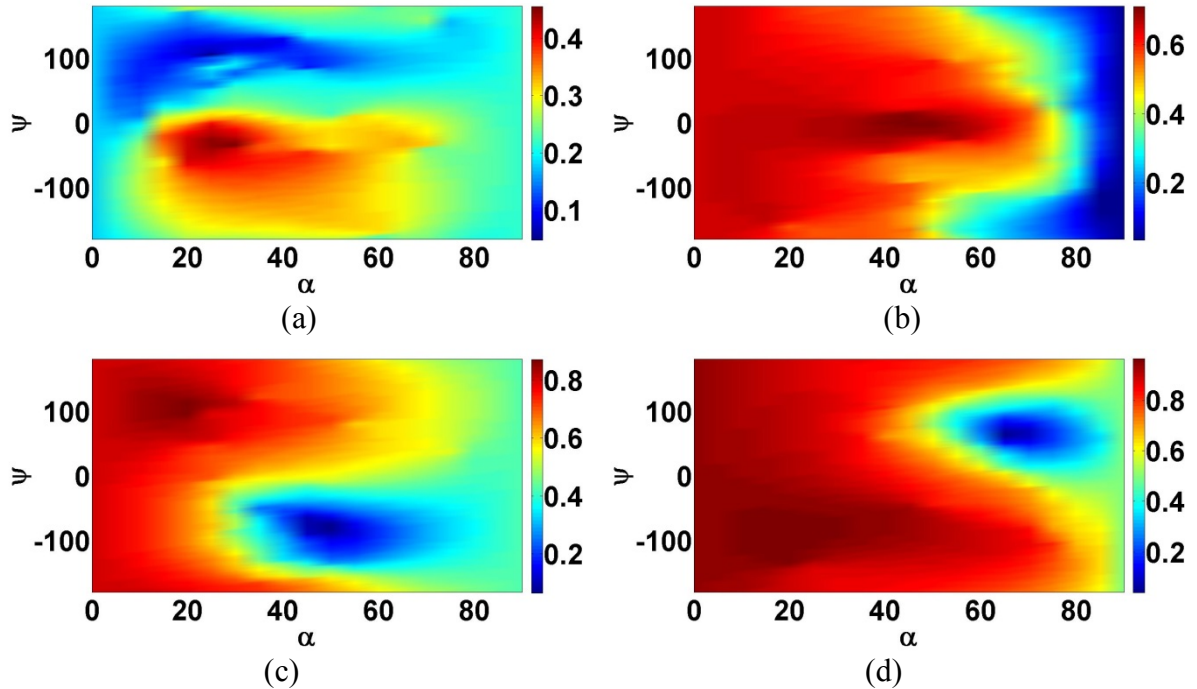


Fig .3. Temporal coherence values as a function of (α, ψ) for four representative pixels with different values of $\gamma_{pol,x}$. (a) $\gamma_{pol,x}=0.456$, (b) $\gamma_{pol,x}=0.711$, (c) $\gamma_{pol,x} =0.871$, (d) $\gamma_{pol,x}=0.962$.

310 Histograms of the estimated $\gamma_{pol,x}$ in PolStaMPS and the estimated γ_x in standard StaMPS for
 311 initial selected pixels are compared in Figure 4. This comparison shows a significant increase
 312 in the number of pixels with high temporal coherence for the optimum channel, compared to
 313 the HH, VV and HH+VV channels. The increase in coherence will be, in part, due to an
 314 increase in the bias. For instance, coherence estimated on the sea is not zero (as it should be
 315 theoretically) due to the estimation bias in any single channel and, moreover, increases in the
 316 optimum polarimetric combination. To test whether the entire coherence increase can be
 317 explained by an increase in the bias, we check (below) the spatial distribution of the optimum
 318 coefficients, and compare the noise levels of selected points in the original channels to those
 319 in the optimum channel. We note, however, that in any case, the increase in bias should not
 320 lead to more pixels being selected, due to the StaMPS mechanism for pixel selection, which
 321 depends on a comparison of the coherence distribution to that for simulated pixels, rather than
 322 simple thresholding.

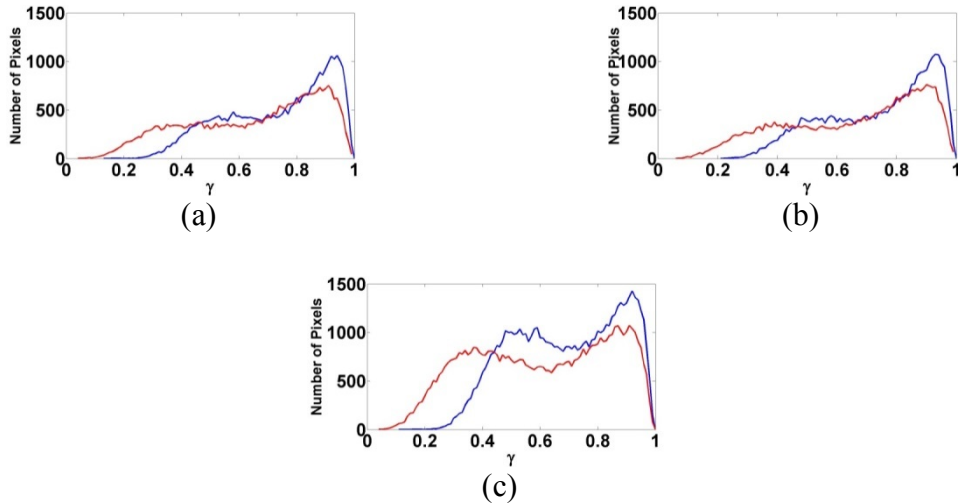


Fig. 4. Histogram of the γ_x and the $\gamma_{pol,x}$ for initial selected pixels related to (a) HH and Optimum channel, (b) VV and Optimum channel, (c) HH+VV and optimum channel. Blue and red line indicate the optimum and single-pol channel behaviour, respectively.

323 In homogeneous areas, the scattering properties of neighbouring pixels are expected to be
 324 spatially similar. Therefore, if the projection vectors and the optimum coefficients reflect the
 325 actual scattering properties, rather than taking values that just increase the coherence bias of
 326 each pixel, they will generally be spatially smooth.

327 As can be seen in Figure 5., the estimated coefficients are not randomly distributed and there
 328 is spatial consistency for the distribution of all coefficients, especially f_1 and f_4 , which are real
 329 numbers and correspond to the two co-polar interferograms. The coefficient of the first co-
 330 polar interferogram, f_1 , which enhances surface scattering behaviour, has large values in most
 331 of the areas. Moreover, a clear complementarity between f_1 and f_4 is observed since where f_1
 332 is small, f_4 is large. f_2 and f_3 are complex coefficients for the two cross-polar interferograms
 333 and their maps are similar for amplitude and phase.

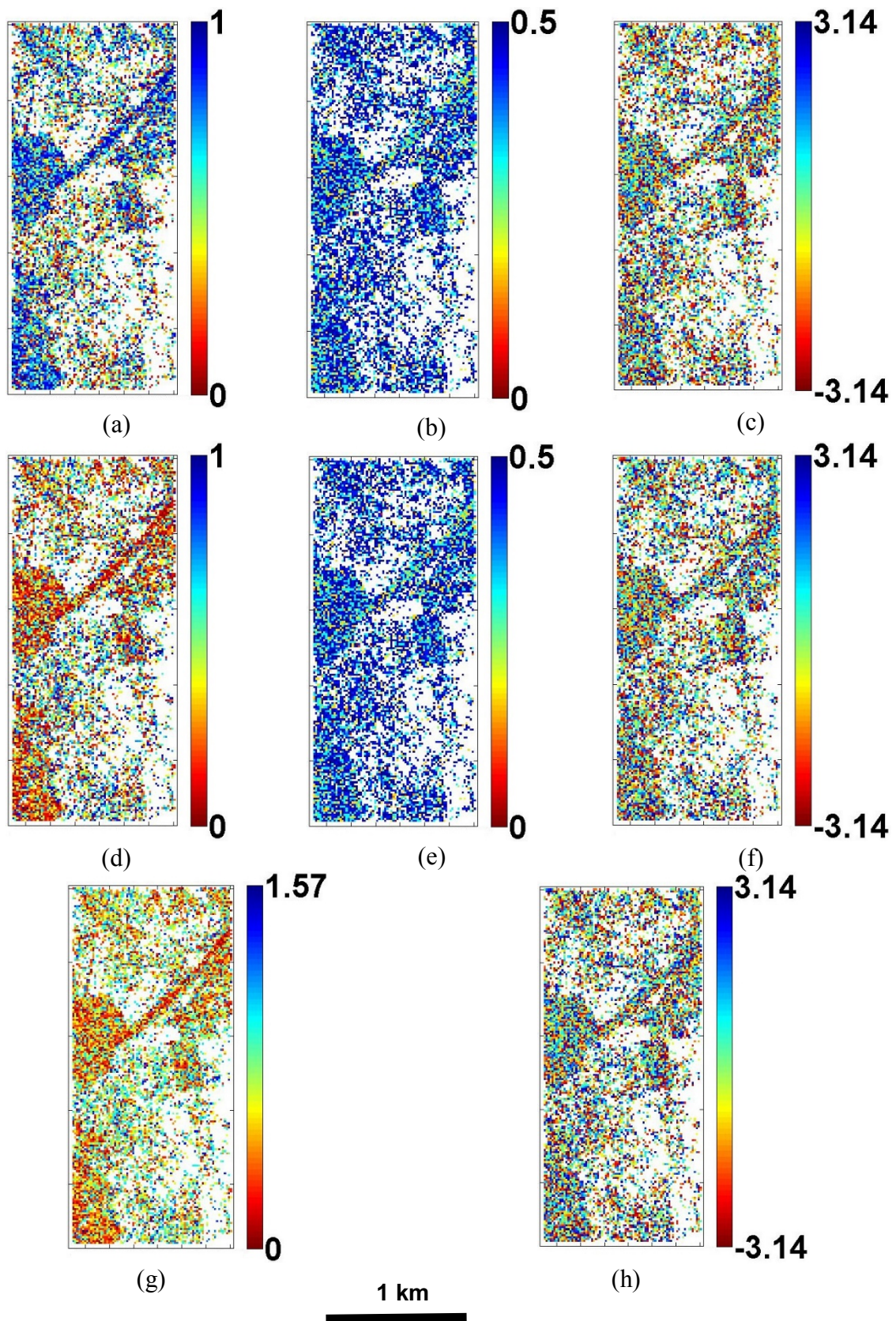


Fig. 5. Maps of optimum coefficients and parameters for an interferogram. (a) f_1 , (b) amplitude of f_2 , (c) phase of f_2 (d) f_4 , (e) amplitude of f_3 , (f) phase of f_3 , (g) α , (h) ψ .

334 The number of final selected PS pixels over the case study using standard StaMPS for different
335 channels (HH, VV, HH+VV) and PolStaMPS is presented in Table. 1. It is clear that the
336 increase in the number of PS pixels using the HH+VV channel in standard StaMPS compared
337 to the linear channels is trivial. However, using PolStaMPS the number increases by 48%, 80%
338 and 82% with respect to HH+VV, VV and HH channel, respectively. There are some PS pixels
339 which are not identified by StaMPS with linear channels, but they are selected by both
340 PolStaMPS and StaMPS with HH+VV. In fact, approximately 40% of the additional PS pixels
341 that are selected by PolStaMPS with respect to StaMPS with linear channels are also selected
342 by StaMPS with HH+VV channel.

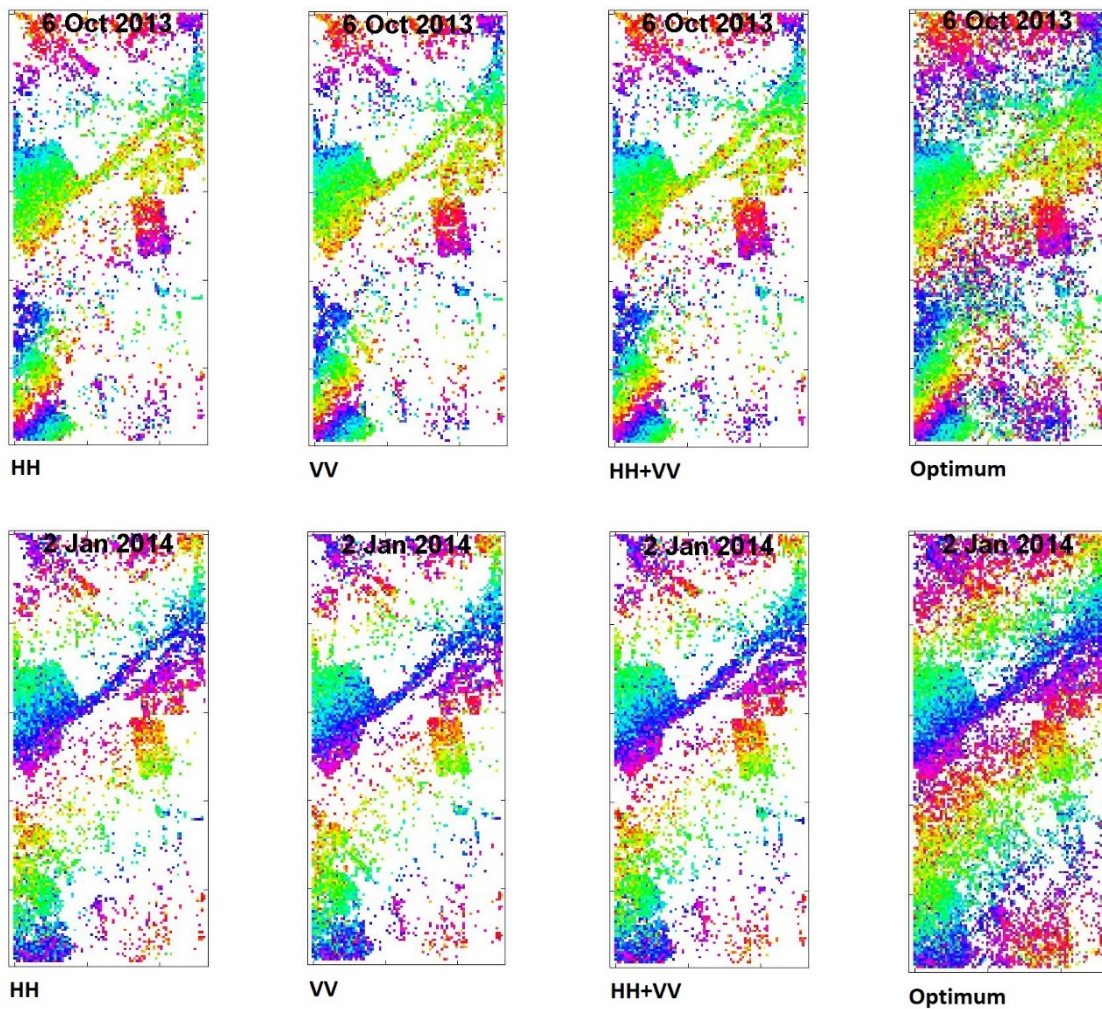
343 **Table 1. Number of identified PS pixels**

HH	VV	HH+VV	Optimum
26322	26694	32374	47997

344 Figure 6 shows the wrapped phase of selected pixels for optimum interferograms and HH, VV
345 and HH+VV interferograms. As can be seen, the additional PS pixels in the optimum channel
346 look clearly coherent. Furthermore, there are some common PS pixels whose phases are less
347 noisy in the optimum interferogram. In order to assess the phase quality for the interferograms
348 obtained by PolStaMPS in comparison to the original StaMPS, phase noise is estimated
349 according to [9]. First, the PS pixels are connected to form a network using Delaunay
350 triangulation. Then for each arc connecting two PS pixels, a weighted-average phase is
351 calculated from the entire time series, and removed from the original phase of the arc, which
352 is then low-pass filtered in time. The resulting phase, with the weighted-average phase added
353 back in, provides an estimate for the smooth underlying signal. Phase noise is estimated by
354 subtracting the smooth phase from the original phase of the arc. Finally, the phase noise of each
355 PS pixel is obtained from the phase noise of its corresponding arcs. Figure 7 shows a
356 comparison of histograms of phase noise standard deviation for commonly identified PS pixels
357 in single-polar and optimum channels. The optimum channel shows a 7%, 16% and 17%

359 reduction in the number of PS pixels with standard deviation above 0.5 radians with respect to
360 HH+VV, VV and HH channel. This confirms that, in addition to increasing PS density, the
361 proposed algorithm is also successful in reducing the noise level of those PS pixels selected by
362 standard StaMPS, although the reduction in the noise level is less pronounced than the increase
363 in the number of selected PS pixels.

364 The resulting velocity maps of PolStaMPS and standard StaMPS are plotted in figure 8. The
365 pattern of deformation rate is very similar, as expected, but the density of measurements is
366 greater in the PolStaMPS case. The maximum velocity for this case study is -139.7 mm/year
367 for the optimum channel.



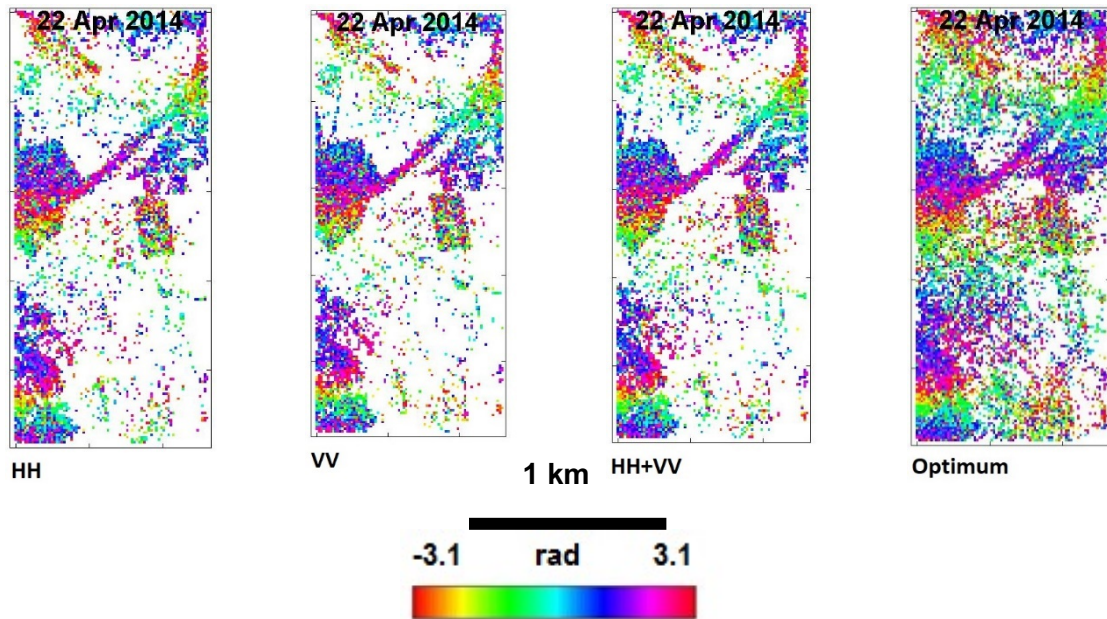


Fig. 6. A selection of wrapped interferograms formed from available data set acquired using HH, VV, HH+VV and Optimum channel over the case study. The master acquisitions date is 11 Dec 2013. Each colour fringe represents 1.55 cm of displacement in the LOS.

368

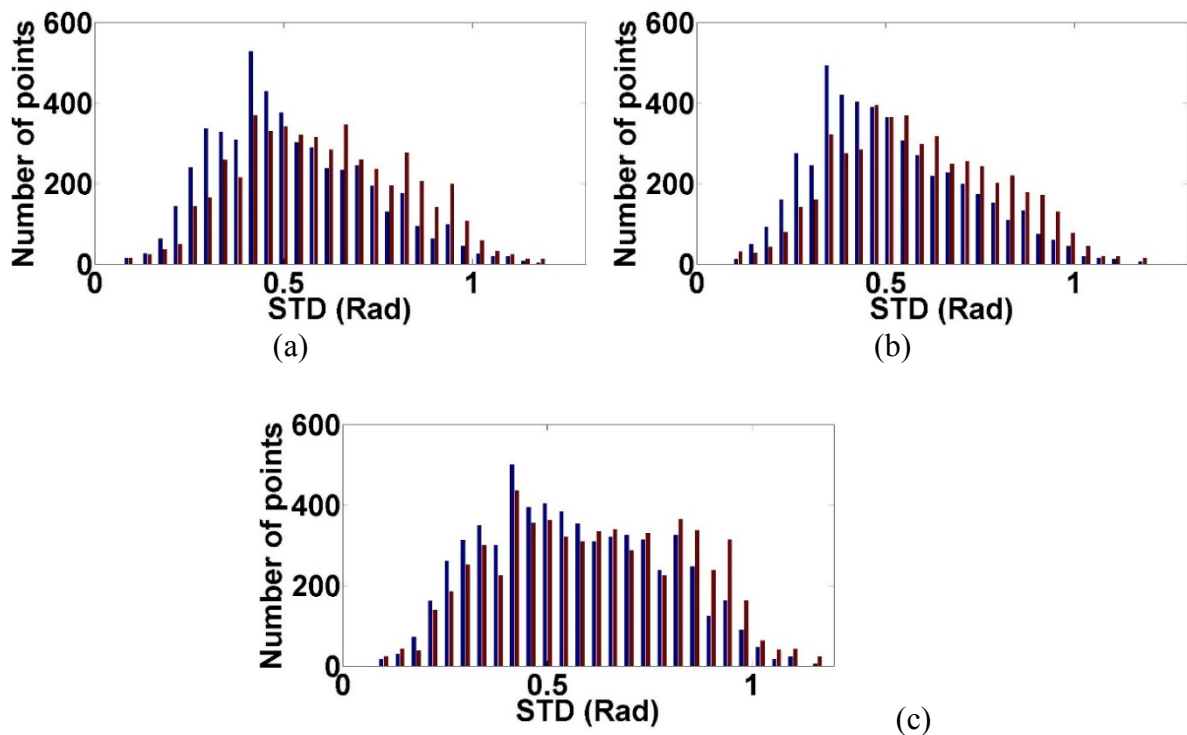


Fig. 7. Histogram of phase noise standard deviation for commonly identified PS pixels between optimum channel and (a) HH channel, (b) VV channel and (c) HH+VV channel. Blue and red bar indicate the optimum and single-polar channel behaviour, respectively.

369

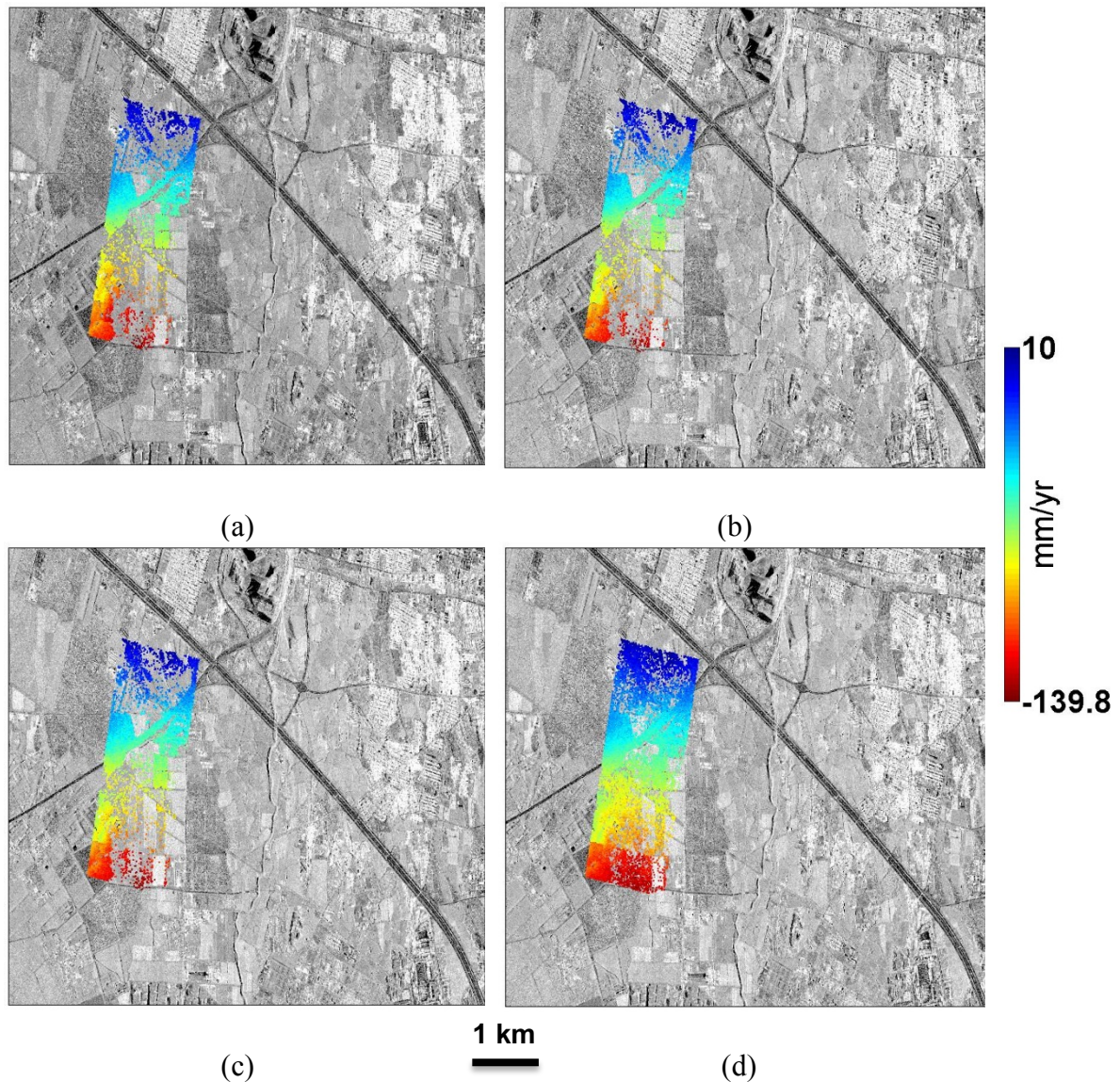


Fig. 8. Mean LOS velocities on the case study between 21 July 2013 and 22 April 2014 plotted on interferogram amplitude, (a) HH channel, (b) VV channel, (c) HH+VV channel, d) optimum channel.

370 The polarimetric PSI method leads to an increase in the number of selected PS pixels when
 371 compared to standard PSI, although this comes with a computational cost. PolStaMPS is
 372 inspired by ESPO and consequently finds the coefficients in the defined search spaces to
 373 optimise the temporal coherence. This leads to an increase in the computation time of ~ 80 times
 374 with respect to standard StaMPS. The computation time depends on the defined step in the
 375 search spaces; larger steps decrease the computation time, although they could lead to
 376 convergence on local optima instead of global ones. Optimising the temporal coherence using
 377 other existing optimisation methods, e.g. Union, in which the optimum channel is selected from

378 a polarimetric channel with limited availability [21], may work with a lower computational
379 cost, but the solutions are suboptimal. It should be mentioned that PolStaMPS can be applied
380 over areas larger than the case study in this research, and the computation cost increases
381 approximately linearly with the number of pixels of the scene.

382 7. CONCLUSIONS

383 In this study, we present a new polarimetric PSI approach that i) is applicable in areas lacking
384 man-made structures and ii) retains the full spatial resolution of the input images. Using this
385 technique we are able to identify natural targets that the standard PSI approach fails to select:
386 the number of PS is improved by 48%, 80% and 82% with respect to the HH+VV, VV and HH
387 channels, respectively. Moreover, the phase quality of the selected PS pixels is also improved.
388 We have successfully applied this new algorithm to a rural part of the Tehran basin to monitor
389 high-rate land subsidence and envisage that it can be used to estimate crustal deformation in
390 most terrains. Future work should include a comparison of the results and performance of
391 PolStaMPS with respect to other polarimetric PSI methods.

392 ACKNOWLEDGMENT

393 All TerraSAR-X images have been provided by DLR in the framework of LAN1335 project.
394 COMET is the NERC Centre for the Observation and Modelling of Earthquakes, Volcanoes,
395 and Tectonics. The work of Juan M. Lopez-Sanchez was supported by the Spanish Ministry of
396 Economy and Competitiveness and EU FEDER under Project TIN2014-55413-C2-2-P, and by
397 the Spanish Ministry of Education, Culture and Sport under Grant PRX14/00151.

398 REFERENCES

- [1] A. Ferretti, C. Prati, F. Rocca, "Permanent scatterers in differential SAR interferometry," *IEEE Trans. on Geosci. and Remote Sensing*, vol. 38, no. 5, pp. 2202-2212, 2000.
- [2] A. Ferretti, C. Prati, F. Rocca, "Permanent scatterers in SAR interferometry," *IEEE Trans. on Geosci. and Remote Sensing*, vol. 39, no. 1, pp. 8-20, 2001.

- [3] C. Colesanti, A. Ferretti, F. Novali, C. Prati, F. Rocca., "SAR monitoring of progressive and seasonal ground deformation using the permanent scatterers technique," *IEEE Transactions on Geoscience and Remote Sensing*, vol. 41, no. 7, pp. 1685-701, 2003.
- [4] S. Lyons, D. Sandwell, "Fault creep along the southern San Andreas from interferometric synthetic aperture radar," *Journal of Geophysical Research*, vol. 108, no. B1, pp. 2047-2070, 2003.
- [5] C. Werner, U. Wegmuller, T. Strozzi, A. Wiesmann, "Interferometric point target analysis for deformation mapping," in *Geosci. and Remote Sensing Symposium, IGARSS*, 2003.
- [6] B. Kampes, Displacement parameter estimation using permanent scatterer interferometry, Delft University of Technology: Ph.D. thesis, 2005.
- [7] P. Berardino, G. Fornaro, R. Lanari, E. Sansosti, "A new Algorithm for Surface Deformation Monitoring based on Small Baseline Differential SAR Interferograms," *IEEE Trans. on Geoscience and Remote Sensing*, vol. 40, no. 11, pp. 2375-2383, 2002.
- [8] R. Lanari, O. Mora, M. Manunta, J. J. Mallorqui, P. Berardino, E. Sansosti, "A Small Baseline Approach for Investigating Deformations on Full Resolution Differential SAR Interferograms," *IEEE Trans. on Geoscience and Remote Sensing*, vol. 42, no. 7, pp. 1377-1386, 2004.
- [9] A. Hooper, H. Zebker, P. Segall, B. Kampes, "A new method for measuring deformation on volcanoes and other natural terrains using InSAR persistent scatterers," *Geophysical Research Letters*, vol. 31, no. 23, 2004.
- [10] R. Bamler and D. Just, "Phase statistics and decorrelation in SAR Interferogram," in *International Geoscience and Remote Sensing Symposium, Geosci. and Remote Sens*, Tokyo, 1993.
- [11] E. Pottier and J.S. Lee, *Polarimetric Radar Imaging: From Basics to Applications*, CRC Press, ISBN 9781420054972, 2009.
- [12] S.R. Cloude, *Polarisation: Applications in Remote Sensing*, Oxford University Press, ISBN 9780199569731, 2009.
- [13] J.S. Lee, M.R. Grunes, R. Kwok, "Intensity and phase statistics of multilook polarimetric and interferometric SAR imagery," *IEEE Trans. Geosci. Remote Sensing*, vol. 32, pp. 68-78, 1994.
- [14] J.J. Van Zyl and C.F. Burnette, "Bayesian classification of polarimetric SAR images using adaptive a priori probability," *Int. J. Remote Sensing*, vol. 13, pp. 835-840, 1992.
- [15] A. Freeman and L. Durden, "A three-component scattering model for polarimetric SAR data," *IEEE Trans. on Geoscience and Remote Sensing*, vol. 36, no. 3, pp. 963-973, 1998.
- [16] J.J. Van Zyl, "Unsupervised classification of scattering behavior using radar polarimetry data," *IEEE Trans. Geosci. Remote Sensing*, pp. 36-45, 1990.

- [17] S.R. Cloude and E. Pottier, "A review of target decomposition theorems in radar polarimetry," *IEEE Trans. Geosci. Remote Sensing*, vol. 34, pp. 498-518, 1996.
- [18] S.R. Cloude and K. P. Papathanassiou, "Polarimetric SAR Interferometry," *IEEE Trans. Geosci. and Remote Sensing*, vol. 36, no. 5, pp. 1551-1565, 1998.
- [19] M. Neumann, L. Ferro-Famil, A. Reigber, "Multibaseline polarimetric SAR Interferometry coherence optimization," *IEEE Geoscience and Remote Sensing Letters*, vol. 5, no. 1, pp. 93-97, 2008.
- [20] E. Colin, C. Titin-Schnaider, W. Tabbara, "An interferometric coherence optimization method in radar polarimetry for high-resolution imagery," *IEEE Trans. on Geosci. and Remote Sensing*, vol. 44, no. 1, pp. 167-175, 2006.
- [21] L. Pipia, X. Fabregas, A. Aguasca, C. Lopez-Martinez, S. Duque, J.J. Mallorqui, J. Marturia, "Polarimetric differential SAR interferometry: First results with ground-based measurements," *IEEE Geosci. Remote Sensing Letters*, vol. 6, no. 1, pp. 167-171, 2009.
- [22] L. Pipia, X. Fabregas, A. Aguasca, C. Lopez-Martinez, J.J. Mallorqui, "Polarimetric coherence optimization for interferometric differential applications," in *IGARSS*, 2009.
- [23] V.D. Navarro-Sanchez, J.M. Lopez-Sanchez, F. Vicente-Guijalba, "A contribution of polarimetry to satellite differential SAR Interferometry: increasing the number of pixel candidates," *IEEE Geosci and Remote Sensing Letters*, pp. 276-280, 2010.
- [24] R. Iglesias, D. Monells, X. Fabregas, J.J. Mallorqui, A. Aguasca, C. Lopez-Martinez, "Phase quality optimization in polarimetric differential SAR interferometry," *IEEE Trans. on Geosci. and Remote Sensing*, vol. 52, no. 5, pp. 2875-2888, 2014.
- [25] Z. Sadeghi, M.J. Valadan Zoej, J.P. Muller, "Monitoring land subsidence in a rural area using a combination of ADInSAR and polarimetric coherence optimization," *IEEE journal of Selected Topics in Applied Earth Observations and Remote Sensing*, vol. PP, no. 99, 2017.
- [26] V.D. Navarro-Sanchez, J.M. Lopez-Sanchez, L. Ferro-Famil, "Polarimetric approaches for Persistent Scatterers Interferometry," *IEEE Trans. on Geosci. and Remote Sensing*, pp. 1667-1676, 2014.
- [27] M. Esmaili and M. Motagh, "Improved persistent scatterer analysis using amplitude dispersion index of dual polarimetry data," *ISPRS Journal of Photogrammetry and Remote Sensing*, vol. 117, pp. 108-114, 2016.
- [28] J.J. Van Zyl, H.A. Zebker, C. Elachi, "Imaging radar polarization signature: theory and observation," *Radio Sci*, vol. 22, pp. 529-543, 1987.
- [29] B. Wu, L. Tong, Y. Chen, L. He, "New methods in multibaseline polarimetric SAR interferometry coherence optimization," *IEEE Geosci. and Remote Sensing Letters*, vol. 12, no. 10, pp. 2016-2020, 2015.

- [30] A. Hooper, P. Segall, H. Zebker, "Persistent scatterer interferometric synthetic aperture radar for crustal deformation analysis with application to Volcan Alcedo, Galapagos," *Journal of Geophysics Research*, vol. 112, 2007.
- [31] A. Hooper, Persistent scatterer RADAR interferometry for crustal deformation studies and modeling of volcanic deformation, Stanford University, Ph.D thesis, 2006.
- [32] M. Amighpey, S. Arabi, A. Talebi, D. Jamour, "Elevation changes of the precise leveling tracks in the Iran leveling network," National Cartographic Center (NCC) of Iran, 2006.
- [33] Z. Sadeghi, M.J. Valadan Zoej, M. Dehghani, "Enhanced algorithm based on persistent scatterer interferometry for the estimation of high-rate land subsidence," *Journal of applied Remote Sensing*, vol. 6, pp. 063573-1-063573-15, 2012.
- [34] Z. Sadeghi, M.J. Valadan Zoej, M. Dehghani, "An improved Persistent Scatterer interferometry for subsidence monitoring in the Tehran basin," *IEEE journal of Selected Topics in Applied Earth Observation and Remote sensing*, vol. 6, no. 3, pp. 1571-1577, 2013.
- [35] M. Dehghani, M.J.Valadan Zoej, A. Hooper, R.Hanssen, I. Entezam, S. Saatchi, "Hybrid conventional and persistent scatterer SAR interferometry for land subsidence monitoring in the Tehran Basin, Iran," *ISPRS Journal of Photogrammetry and Remote Sensing*, vol. 79, pp. 157-170, 2013.